Biomaterials Advances 180 (2026) 214608

Contents lists available at ScienceDirect

Biomaterials Advances

journal homepage: www.journals.elsevier.com/materials-science-and-engineering-c

Development of novel organic/inorganic osteomimetic inks for 3D bioprinted in vitro bone models

Tiziana Fischetti [a,1], Gabriela Graziani [a,2], Giorgia Borciani [a,3], Matteo Pitton [b], Elisa Boanini [c], Nicola Baldini [a,d], Silvia Farè [b,*]

[a] BST Laboratory, Rizzoli RIT-Research, Innovation & Technology Department, Istituto di Ricerca Codivilla Putti, IRCCS Istituto Ortopedico Rizzoli, via di Barbiano 1/10, 40136, Bologna, Italy
[b] Department of Chemistry, Materials and Chemical Engineering "Giulio Natta", Politecnico di Milano, Via Mancinelli 7, 20131, Milan, Italy
[c] Department of Chemistry "Giacomo Ciamician", University of Bologna, Via Francesco Selmi, 2, 40126, Bologna, Italy
[d] Department of Biomedical and Neuromotor Sciences, University of Bologna, via Massarenti 9, 40138, Bologna, Italy

ARTICLE INFO

Keywords:
3D bioprinting
Osteomimetic bioink
GelMA
Hydroxyapatite
In vitro bone model

ABSTRACT

3D bioprinting is a promising strategy to develop predictive 3D in vitro bone models, surpassing the limitations of 2D and in vivo animal models. The 3D bioprinted models can achieve a high level of complexity, effectively mimicking the native bone niche composition. Furthermore, they allow to tailor the 3D structure geometry and enable precise control over pore size and orientation patterns. In this study, gelatin methacryloyl (GelMA) was selected to develop cell-laden 3D structures by 3D printing extrusion-based technology. Different GelMA concentrations (5, 7.5, 10 % *w/v*) were tested in terms of rheological behavior to select the most suitable for the 3D printing process. Then, the printing process parameters (i.e., pressure, extrusion speed) were optimized to obtain reproducible and accurate 3D printed structures. The optimal concentration (GelMA 7.5 %) was then enriched by stoichiometric hydroxyapatite nanocrystals (nHA, 0.1, 0.2, 0.5, and 1 % w/v), to mimic the inorganic component of bone, and evaluated in terms of 3D printing process and stability properties over 14 days, with enhanced stability in GelMA/nHA hydrogels. Osteosarcoma Saos-2 cells were considered for in vitro biological characterization, and no cytotoxic effect was obtained for GelMA and GelMA/nHA hydrogels. Saos-2 cells embedded in printed GelMA and GelMA/nHA bioinks proliferated over the 14 days of the in vitro culture. The developed formulations can be proposed as osteomimetic bioinks for 3D in vitro bone models, suitable for investigating bone disease mechanisms or for drug screening purposes.

1. Introduction

The gold standard for investigating pathogenic mechanisms, biomaterial testing and drug screening are in vivo animal models. However, these models are affected by high costs, low reproducibility, and ethical concerns. Beside these limitations, animal models may fail when transferred to the clinics due to the existing different physiology between animals and humans [1–4]. Thus, alternative in vitro solutions have been developed. Indeed, although in vitro systems lack the complexity of in vivo pathophysiology, they could allow the understanding of some key mechanisms before proceeding to in vivo trials, hence reducing the need to use animals [5]. Among in vitro models, 2D models have been used for decades. However, they do not succeed in mimicking complex physiological environments, leading to simplistic and partially reliable results [6–8]. Conversely, 3D in vitro models are a valid compromise between in vivo and 2D models to mimic the complex 3D tissue microarchitecture and the cell-cell and cell-ECM interactions, thus resulting in more predictive results. Among the existing techniques

* Corresponding author.
E-mail addresses: tiziana.fischetti@ior.it (T. Fischetti), gabriela.graziani@uniroma5.it (G. Graziani), giorgia.borciani@ior.it (G. Borciani), matteo.pitton@polimi.it (M. Pitton), elisa.boanini@unibo.it (E. Boanini), nicola.baldini@ior.it (N. Baldini), silvia.fare@polimi.it (S. Farè).
[1] Present address: Department for Functional Materials in Medicine and Dentistry, Institute of Biofabrication and Functional Materials, University of Würzburg and KeyLab Polymers for Medicine of the Bavarian Polymer Institute (BPI), Pleicherwall 2, D-97070, Würzburg, Germany.
[2] Present address: Department of promotion of Human sciences and quality of life, San Raffaele Rome University, via val di Canutta 247, 00166, Roma, Italy
[3] Present address: RAMSES Laboratory, Rizzoli RIT-Research, Innovation & Technology Department, Istituto di Ricerca Codivilla Putti, IRCCS Istituto Ortopedico Rizzoli, via di Barbiano 1/10, 40136, Bologna, Italy.

https://doi.org/10.1016/j.bioadv.2025.214608
Received 6 October 2025; Received in revised form 22 October 2025; Accepted 10 November 2025
Available online 10 November 2025

to develop 3D in vitro models, including spheroids [9], cell patterning techniques [10] and microfluidic chips [11], 3D printing/ bioprinting is promising, as it enables the development of 3D structures with different materials composition, and high tunability in scaffold shape and in pore structure and dimensions [7,12–15]. This technology is particularly well-suited for developing 3D in vitro bone models, as it allows for the reproduction of the composite nature of bone tissue (i.e., the mix of inorganic and organic phase). This feature is crucial because mimicking the native bone microenvironment enables more accurate results in investigating the mechanisms leading to pathological conditions (e.g., tumour formation [3,16,17]) and conducting drug sensitivity screening studies [18,19].

To date, several studies have investigated the suitability of different 3D printing strategies (i.e., stereolithography, fused deposition modelling, extrusion-based techniques) to develop 3D scaffold-based models mimicking bone tissue microenvironment [3,16,20]. These models have to fulfil different requirements, such as scaffolds biocompatibility, mimicking of native organic and inorganic phase, and degradability adequate to the in vitro investigation period (i.e., up to 14–21 days) [6,21]. The existing studies have evaluated different materials for bone modelling, including alginate/gellan gum [22], polyurethane (PU) [3,7], polyethylene glycol (PEG) [16], poly (L-lactide) (PLLA) [23], collagen [19], gelatin methacryloyl (GelMA) [13,24], possibly loaded with calcium phosphates (CaPs) or hydroxyapatite nanocrystals (nHA) [21,25,26]. In particular gelatin, deriving from the denaturation of native collagen under heating conditions, exhibits limited antigenicity. Furthermore, it maintains the chemical and biological properties of collagen. Indeed, the bioactive sequences of collagen (i.e., arginine-glycine-aspartic acid (RGD) peptide) responsible for good cells adhesion properties are preserved in the gelatin backbone [27]. Gelatin-based hydrogels have been widely investigated in bone tissue applications due to their excellent biological properties and positive effect in supporting osteogenesis [28–31].

Since bone is an organic/inorganic composite, including nHA in in vitro bone models is essential to mimic the mineralized component of the bone's native microenvironment and enhance the biomimicry of the 3D model. Furthermore, previous studies have shown that nHA modulate the behavior of both healthy and diseased cells [27,28]. However, the inclusion of the mineral phase poses some challenges. While the HA content in natural bone is relatively high (approximately 60–70 % of the bone's dry weight [21,32]), the concentration of HA used in 3D printing applications is considerably lower, typically ranging from 1 to 15 % by weight [13,33–35]), with some studies reporting even lower ranges [36,37]. This concentration needs to be carefully tailored based on factors such as the performance of the 3D printing system, the characteristics of the nHA particles themselves, and the properties of the hydrogel used in combination with the nHA particles. Another concern with the inclusion of the nHA in in vitro bone models is that many studies [34,38–40] use commercial nHA, which exhibits high variability in composition (including the presence of CaP phases different from HA) and morphology, while the use of CaPs nanocrystals with control over the composition, crystallinity degree and crystals dimensions is needed to achieve predictable and reproducible behavior in the models [41,42]. Moreover, among the existing studies on 3D bone printing for developing in vitro bone models, only a few [13,17,18] focus on 3D bioprinting of biomimetic nanoparticles. These studies indicate that this approach promotes cell colonization throughout the scaffold and allows control over spatial distribution [13,43–45]. In this framework, extrusion-based bioprinting is more suitable than stereolithography and fused deposition modelling technologies, as it enables printing a bioink including living cells and biomaterials with inorganic micro- or nano-fillers playing as bioactive components, thus better replicating cell-cell and cell-ECM interactions. To allow bioprinting of bone models recapitulating the bone niche microenvironment, customized bioinks shall be developed, with suitable characteristics in terms of viscosity, printability and shape fidelity. Indeed, the bioink should show a shear-thinning behavior [46,47], thus resulting in a non-viscous fluid during the extrusion process and behaving as a stable gel after the 3D bioprinting process. Moreover, the 3D bioprinting process and the bioink composition should provide a cell-friendly environment, in which the encapsulated cells show high viability after the process and over all the investigation period, that normally range from 1 to 14 days [48–51]. This is particularly relevant when incorporating a ceramic phase in the ink, that could increase shear stress and cause cells damage [52–54].

In the present study, we focused on the development of an osteomimetic ink in which the organic and inorganic phases can mimic bone composition, evaluating its suitability for a 3D extrusion-based bioprinting approach. As organic phase, GelMA [34] was investigated in terms of rheological behavior, 3D printing process and parameters optimization. Non-commercial stoichiometric nHA was synthesized and considered at different concentrations as inorganic component in the GelMA bioink. The GelMA/nHA hydrogels were evaluated in terms of rheological properties, and printing process/parameters. The inclusion of nHA, besides increasing the model biomimicry, was expected to allow further tuning of the rheological properties on the ink and had a positive effect in terms of printing accuracy and shape fidelity [13,34,35,51]. After selecting the most promising inks combination, we combined these formulations with Saos-2 osteosarcoma cells. While GelMA/nHA bioinks have demonstrated compatibility with various cell lines in previous studies [51,55,56], in this study we propose the investigation on 3D bioprinting Saos-2 osteosarcoma cells. As Saos-2 cells derive from osteosarcoma, this cell type is particularly relevant for studying bone-related diseases and testing therapeutic strategies. Consequently, the results obtained in our study hold directly applicability for developing 3D bioprinted in vitro bone models, which are essential for advancing research in in vitro diseased models and drug screening applications.

2. Materials and methods

2.1. Materials

Gelatin (porcine skin, type A), methacrylic anhydride, Dulbecco's phosphate buffered saline (DPBS) and photoinitiator 2-hydroxy-1-(4-(hydroxy ethoxy) phenyl) -2-methyl-1-propanone (Irgacure 2959) were purchased from Sigma Aldrich. Iscove's Modified Dulbecco's Medium (IMDM, Gibco, Thermo Fisher Scientific), fetal bovine serum (FBS), penicillin/streptomycin solution (P/S, penicillin 10,000 units/mL, and streptomycin 10 mg/mL, P/S) and trypsin/EDTA (Trypsin 0.05 %-EDTA 0.02 % in PBS) were purchased from EuroClone S.p.A. AlamarBlue Cell Viability Reagent and Live/Dead Cell Imaging Kit (488/570) were purchased from ThermoFisher Scientific. nHA was synthesized following a procedure described elsewhere [57,58].

2.2. Synthesis of GelMA and nHA addition

GelMA synthesis was performed by dissolving 10 % *w/v* of gelatin in DPBS solution at 50 °C [59]. After complete dissolution, 0.8 mL methacrylic anhydride per gram of gelatin were added under constant stirring conditions. Then, the reacted solution was four-fold diluted by adding pre-heated (T = 37 °C) DPBS and dialyzed against dH2O for 7 days (12–14 kDa cut-off dialysis tubing) to eliminate unreacted methacrylic anhydride and salts. The solution was filtered through filtration units (pores dimension = 0.22 μm), lyophilized, and stored at −20 °C until further use. To prepare the inks, the freeze-dried GelMA (5, 7.5 and 10 % *w/v* concentration) was mixed at 50 °C in DPBS, containing 0.5 % w/v Irgacure 2959. Then, nHA has been added to the DPBS solution where GelMA was dissolved. Thus, the nHA concentrations (0.1, 0.2, 0.5 and 1) are expressed as % (*w/v*) respect to the total volume solution (i.e., GelMA + DPBS). To homogeneously distribute the nHA particles within the GelMA + DPBS solution, sonication (Sonorex Super 10P, Bandelin, Germany) for 10 min was performed.

2.3. In vitro cytotoxicity of GelMA w/wo nHA inks

Saos-2 human osteosarcoma cells were purchased from ATCC (cell line BS TCL 90, ATCC, Rockville, MD). Cells were maintained in IMDM supplemented with 1 % P/S and 10 % FBS, in incubator (37 °C, 95 % humidity and 5 % CO_2). For passaging, trypsin/EDTA was used. The culture medium was refreshed every 3 days. Cells at 80 % of confluence were trypsinized and used for the following experiments:

a) effects of UV lamp (crosslinking method) on Saos-2 cells metabolic activity to detect potential cytotoxic effects caused by the UV crosslinking. Saos-2 cells were seeded (cell density = 5×10^3 cells/well) in a 24 well tissue culture polystyrene plate (TCPS) and the adhesion was allowed to obtain "cell adherent" samples. Then, 5×10^3 Saos-2 cells were seeded and, before cells adhere to TCPS (samples labelled as "cell suspension" samples), 0.7 mW/cm^2 UV lamp (VL-6.L 365 nm, power UV tube 6 W, Vilber Lourmat, France) was used for 5 min at a distance of 3 cm from the samples. Saos-2 cells adherent to TCPS and maintained in fresh medium were used as control (CTRL). Cell metabolic activity was evaluated after 1, 2 and 3 days of maintenance.
b) effects on cell metabolic activity of by-products potentially released from GelMA 7.5 % ink when maintained in IMDM in incubator (37 °C, 95 % humidity and 5 % CO_2) for 1 day (conditioned medium, CM). The cell seeding density was the same as in (a) and, after 1 day in culture, culture medium was replaced with 500 μL/well CM and cell metabolic activity was evaluated.
c) metabolic activity of Saos-2 cells manually mixed with GelMA 7.5 %, GelMA 7.5 %/0.1 nHA, and GelMA 7.5 %/0.5 nHA inks. Saos-2 cells (cell density = 5×10^3 cells/10 μL) were embedded in 50 μL of the considered formulations and poured in PDMS molds (Ø = 4 mm, h = 2.5 mm).

After performing the crosslinking process (0.7 mW/cm^2 UV lamp, t = 5 min, at a distance of 3 cm from the the samples), samples were maintained in IMDM in incubator (37 °C, 95 % humidity and 5 % CO_2) and cell metabolic activity was analysed at 1, 3, 7 and 14 days to evaluate potential cytotoxic effects of GelMA 7.5 % and GelMA 7.5 %/nHA bioinks.

2.4. Rheological characterization

The rheological behavior of GelMA w/wo nHA inks (GelMA 5 %, 7.5 %, 10 %, GelMA 7.5 %/0 nHA, 0.1 nHA, GelMA 7.5 %/0.2 nHA, GelMA 7.5 %/0.5 nHA, GelMA 7.5 %/1 nHA) was evaluated by a rotational rheometer (MCR 302 Modular Compact Rheometer, Anton Paar GmbH, Austria) equipped with parallel plates (Ø = 25 mm, gap between plates = 0.5 mm). Samples (250 μL) were positioned on the lower plate and upper plate was lowered to start the measurement (n = 2 per each). Silicon oil was added to avoid samples drying. Shear rate sweep tests ($\dot{\gamma}$ = 0.1–1000 s^{-1}) were initially performed on GelMA solutions at different concentrations (5, 7.5, 10 % *w/v*) by varying the temperature of the test (T = 16, 22, 24 °C). Shear rate tests were then carried out on GelMA solutions (7.5 %, 10 % w/v) by adding nHA at different concentrations (0, 0.1, 0.2, 0.5, 1.0 % w/v) and maintaining constant measurement temperature (T = 22, 24 °C). Prior to the test, samples were preconditioned ($\dot{\gamma}$ = 0.1, f = 1 Hz for 60 s, and rest condition for 60 s). Shear thinning behavior of GelMA solution (7.5 %, 10 % w/v) formulations added with nHA was computationally elaborated by considering the Herscher-Bulkley model, by fitting a non-linear curve along the shear rate vs shear stress curve originated from the rheological tests. Herschel-Bulkley model can be summarized as in Eq. (1):

$$\tau(\dot{\gamma}) = \tau_0 + K\dot{\gamma}^p \quad (1)$$

where τ_0 = yield point, p = flow index, K = consistency index. The p index describes the behavior of the bioink: if $p = 1$, Newtonian fluid; if $p > 1$, pseudoplastic material; if $p < 1$, shear-thinning material.

2.5. 3D printing optimization of GelMA w/wo nHA inks

Before performing the 3D printing process, GelMA 5 %, 7.5 % and 10 % were tested for extrudability through a 22 G needle (inner diameter = 410 μm) at different temperatures (16, 22, 24 °C). The ink flow was assessed empirically, by extruding the gel throughout the needle (pressure range 10–40 kPa) using an extrusion-based bioprinter (BioX, CELLINK, Sweden). Based on the obtained results, GelMA 7.5 % and GelMA 7.5 %/nHA were considered to develop the 3D printed structures. A four-layer scaffold with 0–90° pattern geometry (10*10*1.64 mm^3) and 45 % infill density was designed, according to previous studies on 3D structures for bone applications [27,60,61]. The 3D printing process was performed by setting the print-head and the print-plate temperature at 22 and 12 °C, respectively. Different printing parameters were evaluated, and in particular 17, 23, 29 kPa for the extrusion pressure and 4, 7, 10 mm/s for the deposition speed. After the optimization process, the extrusion pressure and the deposition speed were set to 23 kPa and 7 mm/s, respectively. A pre-flow of 2000 ms was set before starting the 3D printing of each structure, to enable the material reaching the needle tip. The obtained 3D printed structures were photo-crosslinked by UV lamp (λ = 365 nm, t = 5 min, distance from the UV source = 3 cm).

To calculate the 3D printing accuracy, top-view images of the scaffold fiber diameters and pores dimensions (n = 3 samples) were acquired by optical stereomicroscopy (SM Z 18 Zoom Body Nikon, Nikon Europe B.V., The Netherlands) and analysed by ImageJ software (version 1.53a). The obtained measurements were compared to the theoretical ones, by using Eq. (2):

$$Accuracy\ [\%] = \frac{1}{n} * \sum_{1}^{n} \left(1 - \frac{|d_r - d_s|}{d_s}\right) * 100 \quad (2)$$

where: n = is the number of the considered samples, d_r = obtained fiber diameter, d_s = theoretical diameter (i.e., 410 μm for 22 G needle).

2.6. In vitro stability test

Stability behavior was evaluated on the 3D printed samples (n = 3 for each condition, specifically GelMA 7.5 %, GelMA 7.5 %/0.1 nHA and GelMA 7.5 %/0.2 nHA) by measuring the residual weight (RW (%)) of samples after incubation in dH2O and complete IMDM at pH 7.4. The residual weight was calculated at different time points (t = 1 h, 1, 3, 7, and 14 days), by using Eq. (3):

$$RW\ (\%) = \frac{W_t}{W_0} \times 100 \quad (3)$$

where Wt = sample weight at the selected timepoint and W_0 = sample weight immediately after 3D printing process. The obtained RW (%) results were plotted as mean value ± standard deviation versus time for the considered formulations.

2.7. 3D bioprinting process

3D bioprinting process was performed using GelMA 7.5 % and GelMA 7.5 %/0.2 nHA inks and Saos-2 cells (10×10^6 Saos-2 cells/mL). Constructs (0–90° pattern geometry, 10*10*1.64 mm^3 dimensions and 45 % infill density) were bioprinted using the optimized parameters (see Results). After performing the crosslinking process, samples were maintained in complete IMDM in incubator (37 °C, 95 % humidity and 5 % CO_2) up to 14 days, with medium refresh every 3 days. Cell metabolic activity was evaluated by Alamar Blue assay and Live Dead assay at 1, 3, 7 and 14 days, according to the manufacturer's instructions. For the one-step Alamar Blue assay, the culture medium was removed and replaced with 10 % (*v*/v) of Alamar Blue solution in IMDM, and incubated (37 °C,

95 % humidity and 5 % CO_2) for 4 h. The fluorescence of Alamar Blue solution was quantified by using a microplate reader (Infinite F200 PRO, TECAN, Switzerland) at $\lambda_{excitation} = 535$ nm and $\lambda_{emission} = 590$ nm. The results are expressed as Relative Fluorescence Units (RFU). For each formulation and timepoint, the result is calculated using Eq. (4) by averaging the fluorescence values on $n = 5$ bioprinted constructs for each type of hydrogel ($RFU_{Bioprinted\_constructs}$). Each construct was measured in triplicate.This average is then adjusted by subtracting the background, i.e, the fluorescence from the cell-free material (RFU_{Cell_free}). The data are reported as mean value ± standard error of triplicates.

$$RFU = RFU_{Bioprinted\_constructs} - RFU_{Cell\_free} \quad (4)$$

Cell viability was evaluated by Live/Dead Cell Imaging kit at day 1, 3, 7 and 14, according to the manufacturer's protocol. Briefly, samples ($n = 3$, for each timepoint) were washed with DPBS and incubated in the dark (37 °C, 95 % humidity and 5 % CO_2) with the live/dead staining mixture for 15 min. Samples were observed by fluorescence microscopy (ECLIPSE E800, Nikon) and cells viability was obtained by counting the number of live (green) ($N_{viable\ cells}$) and dead (red) ($N_{dead\ cells}$) cells in five fields (20 x magnification) for each sample, by Fiji (ImageJ) software [62]. The percentage of cell viability was calculated as in Eq. (5):

$$Cell\ viability\ [\%] = \frac{N_{viable\ cells}}{N_{viable\ cells} + N_{dead\ cells}} * 100 \quad (5)$$

Cell viability data are reported as mean value ± standard error for each formulation and timepoint.

2.8. Statistical analysis

The results obtained by 3D printing optimization are reported as mean ± standard deviation, while in vitro biological results are indicated as mean ± standard error. Statistical analyses among the experimental groups and the time- points were accomplished by the non-parametric Mann–Whitney test for unpaired data [63] and, where appropriate, by the Wilcoxon test for paired data, using GraphPad Prism 8 software. The following significances were considered: p-value ≤0.05 = *, $p \leq 0.01$ = **, $p \leq 0.001$ = ***, $p \leq 0.0001$ = ****.

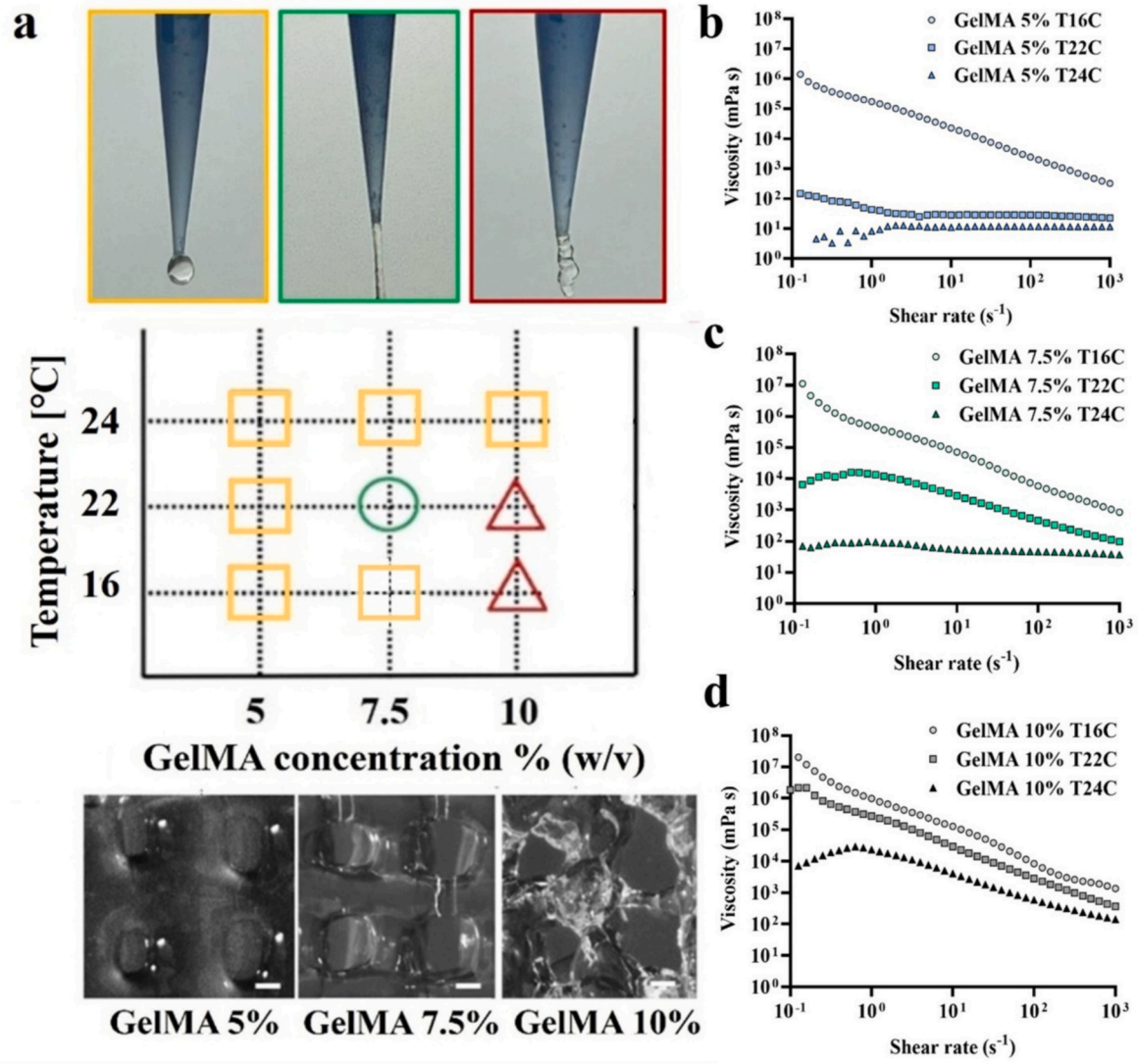

Fig. 1. Selection of GelMA concentration and rheological characterization. **(a)** Effect of selected temperatures on GelMA concentrations (5,7.5, 10 % *w/v*) during the extrusion process. Scaffold images are obtained by stereomicroscope. Magnification: 1×. Scale bar: 500 μm. Viscosity versus shear rate plots evaluated at $T = 16$ °C, 22 °C, 24 °C for **(b)** GelMA 5 %, **(c)** 7.5 % and **(d)** 10 %.

3. Results

3.1. 3D printing and characterization of GelMA hydrogel

Different GelMA concentrations (5, 7.5 and 10 % *w/v*) were evaluated in terms of extrudability at different temperatures (16 °C, 22 °C, 24 °C) (Fig. 1(a)). The GelMA concentrations and temperatures were selected from the literature [27,60,64,65] and empirically tested in terms of extrudability. Literature reports that sol-gel transition temperature is ≈ 20–21 °C for GelMA 5 %, and ≈ 24 °C for GelMA 10 % [27,66,67]. GelMA is characterized by a thermo-responsive behavior, thus it behaves as a liquid-like state above the sol-gel transition temperature, and as a gel-like state below this temperature. Therefore, a temperature below the sol-gel transition is required on the platform during extrusion-based 3D printing process. To be eligible for extrusion-based 3D printing, the material should be extruded smoothly through the needle and should retain the printed shape when deposited on the substrate. Insufficient viscosity, gelling behavior and/or impossibility to extrude continuous fibers hamper the 3D printing process. In this study, GelMA 5 % behaved as a weak gel near the sol-gel transition temperature ($T = 22$ °C and 24 °C), leading to droplet formation at the needle tip (Fig. 1(a)). Consequently, obtaining stable fibers was difficult. Conversely, GelMA 10 % was too viscous to be extruded at 16 °C and 22 °C, resulting in irregular fragments rather than homogeneous fibers (Fig. 1(a)). Although extrusion improved at 24 °C, frequent needle clogging occurred. GelMA 7.5 % exhibited better behavior, enabling the extrusion of continuous and homogeneous fibers, particularly at 22 °C (Fig. 1(a)).

To validate these findings, the viscosity behavior of GelMA 5 %, 7.5 %, and 10 % was evaluated at 16 °C, 22 °C, and 24 °C (Figs. 1(b), (c), (d)). As observed, viscosity decreases with increasing temperature, with this effect being more pronounced at higher GelMA concentrations (from 5 % to 10 % w/v). This temperature-dependent behavior is critical for optimizing 3D printing process, as both excessively low and high viscosity negatively affect bioink printability.

GelMA 5 % showed no shear-thinning behavior at 22 °C and 24 °C, a key requirement for extrusion-based 3D printing. At 16 °C, viscosity was too high at low shear rates, preventing flow and extrusion.

GelMA 10 % exhibited shear-thinning behavior across all tested temperatures (shear rate sweep: 0.1–1000 s^{-1}). However, at 16 °C and 22 °C, viscosity was too high at low shear rates, preventing extrusion. At 24 °C, viscosity decreased sufficiently to allow extrusion through the nozzle.

GelMA 7.5 % showed low viscosity and no shear-thinning behavior at 24 °C, whereas shear-thinning was observed at both 16 °C and 22 °C. However, at 16 °C, viscosity was still too high at low shear rates for successful extrusion.

Although GelMA 7.5 % at 22 °C and GelMA 10 % at 24 °C exhibited similar viscosity and shear-thinning behavior, GelMA 10 % was discarded due to frequent needle clogging during 3D printing, an issue not observed with GelMA 7.5 %. Therefore, GelMA 7.5 % was selected as the most suitable concentration for 3D printing process and was further characterized.

To optimize the 3D printing process, different values of pressure (17, 23, 29 kPa) and deposition speed (4, 7, 10 mm/s) parameters were evaluated (Fig. 2(a)).

As expected, a strong correlation was found between pressure and deposition speed. Indeed, too high (29 kPa) or too low (17 kPa) values of pressure (vs speed, 4 mm/s and 10 mm/s) led to excessive or insufficient GelMA hydrogel deposition, respectively (Fig. 2(a)). The other combinations enabled the obtainment of defined fibers. However, in this study, 23 kPa extrusion pressure and 7 mm/s deposition speed were selected as the optimized parameters to obtain reproducible and accurate 3D structures (Fig. 2(a)). To enhance physical gelation and support the shape fidelity maintenance after fiber deposition [60,68], the printing platform temperature was cooled down to $T = 12$ °C (i.e., below

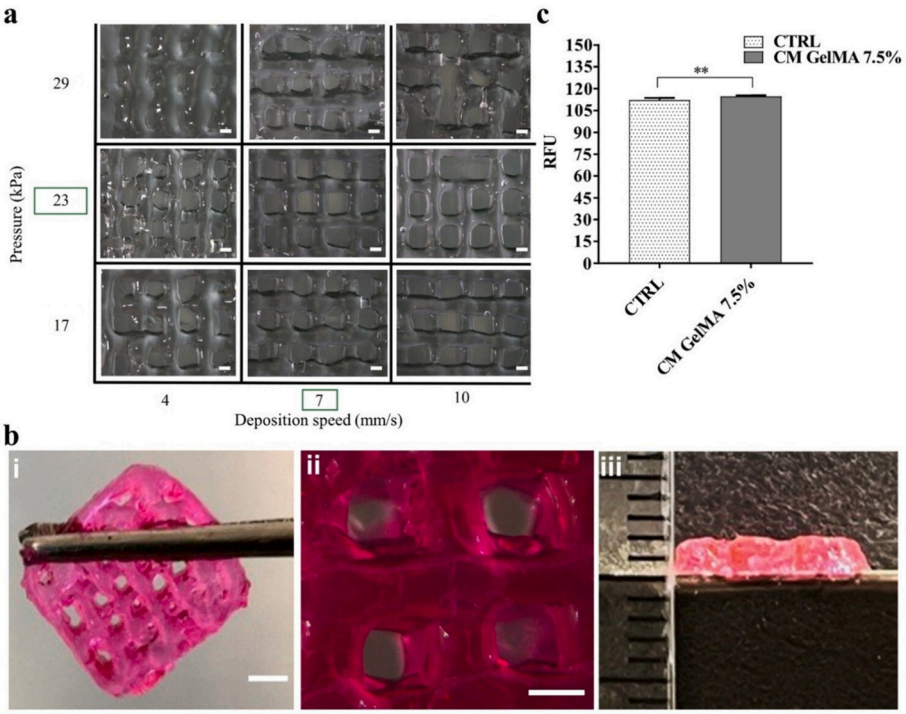

Fig. 2. GelMA printability assessment and cytotoxicity evaluation. **(a)** Stereomicroscope images (1×) of GelMA fibers by varying extrusion speed and deposition speed parameters. The green square highlights the optimal pressure-speed combination. Scale bar = 500 μm. **(b) (i)** Macroscopic image of the 3D printed scaffold. Scale bar = 2 mm **(ii)** top-view of the pores obtained by stereomicroscope (2×), scale bar = 500 μm, and **(iii)** side view of the 3D printed scaffold. **(c)** Saos-2 cells metabolic activity after 1d culture in CM derived from GelMA 7.5 %. (For interpretation of the references to colour in this figure legend, the reader is referred to the web version of this article.)

the sol-gel transition temperature).

After the 3D printing process, samples were UV crosslinked. The selected crosslinking process did not cause any cytotoxicity to the embedded cells, as shown in the Supplementary Material (figure SM1).

The 3D structures were then quantitatively evaluated in terms of printing fidelity and suitability as bone tumour models. The average dimension of fibers was measured after UV crosslinking of the 3D printed structures, being 509 ± 38 μm (Figs. 2(b), i, ii). The printing accuracy evaluated comparing the fiber diameter dimensions to the needle size (i.e., 410 μm) was acceptable [69], being 76 ± 9 %. The discrepancy between fiber diameter and needle size can be attributed to a partial relaxation behavior occurring upon deposition during the 3D printing process [70]. Indeed, correspondingly, the total height of the 3D printed scaffold (≈ 1.61 ± 0.14 mm, Fig. 2(b), iii) is slightly lower (1.8 %) than the expected dimension (1.64 mm).

A preliminary biological evaluation of GelMA 7.5 % was performed to understand if the possible by-product release by GelMA 7.5 % might exert potentials cytotoxic effects on Saos-2 cells. When compared to the CTRL maintained in fresh IMDM, GelMA 7.5 % did not show any cytotoxic effects in terms of decrease of cell metabolic activity (Fig. 2(c)).

3.2. 3D printing and characterization of GelMA/nHA hydrogel

The rheological behavior of the hydrogel loaded with stoichiometric nHA is reported in Fig. 3. Similar to GelMA 7.5 % alone, the viscosity behavior at different temperatures (T) and the 3D printing parameters were evaluated. As shown in Figs. 1(b), (c), and (d), temperature significantly influences viscosity behavior. At 22 °C (Fig. 3(a)), the addition of nHA has a stronger impact on bioink viscosity compared to 24 °C (Figure SM2). At 24 °C, all formulations exhibit lower viscosity, likely due to the thermosensitive nature of GelMA, which facilitates structural relaxation.

Conversely, at 22 °C, the viscosity trend indicates that nHA addition increases GelMA viscosity, with a more pronounced effect at 0.1 %, 0.5 %, and 1 % *w/v* nHA. However, all nHA concentrations exhibit pronounced shear-thinning behavior, with viscosity decreasing steeply from approximately 0.2 s^{-1} for GelMA 7.5 % with 0.1 %, 0.5 %, and 1 % nHA, and from approximately 0.3 s^{-1} for GelMA 7.5 % with 0 % or 0.2 % nHA, continuing up to 1000 s^{-1}.

To quantify the degree of shear-thinning, the p-index from the Herschel-Bulkley model was calculated (Table SM1, a). This index quantifies the extent of shear-thinning, where a lower p-index indicates stronger shear-thinning behavior and, consequently, improved printability [71].

Although the viscosity values for 0.1 %, 0.5 %, and 1 % nHA are similar, the presence of 0.5 % and 1 % nHA hindered the 3D printing process (particularly at 1 % nHA), even at 24 °C, despite the lower viscosity (Figure SM2). Conversely, 0.1 % and 0.2 % nHA resulted in minimal needle clogging and facilitated the extrusion of highly stable filaments, an effect even more pronounced compared to pristine GelMA 7.5 % (Figs. 3(b), (c)). Although GelMA 10 % was not selected for further experimental development due to frequent needle clogging observed in preliminary trials, additional rheological measurements were conducted for comparison with GelMA 7.5 %. These data show a more pronounced or similar shear-thinning behavior (Table SM1, b) for GelMA 10 % formulations at 22 °C and 24 °C (Figure SM3, a, b) compared to GelMA 7.5 %. However, the higher viscosity observed at low shear rates for GelMA 10 %, particularly upon addition of nHA, may influence the hydrogel extrusion throughout the needle.

These findings confirm that shear-thinning alone is not a sufficient predictor of printability; and other physical parameters (e.g., dynamic viscoelasticity, and surface tension) also play critical roles in determining extrusion performance [46].

Regarding p-index for GelMA 7.5 %, these were lower for all GelMA 7.5 % formulations at 22 °C compared to 24 °C, confirming that stronger shear-thinning behavior occurs at lower temperatures and can enhance printability. However, temperatures below the optimal range (e.g., 16 °C) caused excessive gelation and stiffness, which impaired extrusion. These results highlight the existence of a temperature-dependent printability window, where optimal shear-thinning can be achieved without the material becoming either too solid or overly fluid.

Before proceeding with further investigations, a preliminary biological evaluation of GelMA 7.5 %/0.5 nHA and GelMA 7.5 %/0.1 nHA was performed to assess if the addition of nHA might exert potentials cytotoxic effects on Saos-2 cells. No cytotoxic effects were detected (figure SM4, SM5); in fact, an increase in cell metabolic activity was observed in presence of nHA in comparison to CTRL (absence of nHA).

Regarding printing parameters, the pressure values for GelMA 7.5 %/0.1 nHA and GelMA 7.5 %/0.2 nHA were increased to 25 and 26 kPa, respectively (vs 23 kPa for GelMA 7.5 %), with the deposition speed at 7 mm/s. For GelMA 7.5 %/1 nHA, the increase in pressure values was not helpful to extrude the filament due to the needle clogging (Fig. 3(c)). Thus, there is a nHA limit concentration that can be added to GelMA hydrogel; in fact, above a certain concentration, nHA addition was detrimental for extrusion 3D printing process. Indeed, although the printing of 3D GelMA 7.5 %/0.5 nHA structures was possible, the needle clogging was frequent and resulted in non-continuous extruded filaments, thus impairing the obtainment of coherent 3D printed structures (Figs. 3 (b), (c)). Thus, 0.5 % nHA was considered as the limit concentration for printability. To further characterize the bioinks, a preliminary biological assessment of the bioinks was performed and cell metabolic activity of Saos-2 manually mixed in GelMA 7.5 % and up to GelMA 7.5 %/0.5 nHA inks was evaluated. Over time, a positive trend in cell metabolic activity was observed across all conditions, confirming the healthy state of embedded cells and the absence of cytotoxic effects (figure SM4, SM5). However, there was a significant difference ($p \leq 0.001$) in the metabolic activity of Saos-2 between GelMA 7.5 %/0.5 nHA and GelMA 7.5 %/0.1 nHA.

For GelMA 7.5 %/1 nHA, the fiber extrusion was challenging and the nHA were agglomerating, creating clogs and resulting in their non-homogenous distribution within GelMA fibers. This led to the extrusion of material fragments and severe needle clogging, thus resulting in the printing of incomplete grids (Figs. 3(b), (c)). Based on the extrusion results and preliminary biological assessment up to GelMA 7.5 %/0.5 nHA, GelMA 7.5 %/0.5 nHA and GelMA 7.5 %/1 nHA were not further considered.

The fiber diameter dimensions of GelMA 7.5 %/0.1 nHA and GelMA 7.5 %/0.2 nHA were measured to assess how adding nHA affects printing accuracy compared to GelMA alone. These measurements were then compared to the theoretical diameter (i.e., fiber needle size, 410 μm). The findings, reported in Fig. 3 (d) and (e), indicate that incorporating nHA leads to improved printing accuracy, with a more significant enhancement ($p \leq 0.05$) observed as the nHA concentration increases.

The residual weight of the 3D printed GelMA scaffolds w/wo nHA addition was evaluated by incubating the samples at 37 °C up to 14 days, in dH2O (Fig. 4(a)) and in culture medium (Fig. 4(b)).

The 3D printed structures incubated in dH2O showed a decrease in weight mostly at the early timepoints ($p \leq 0.01$), due to the dissolution of uncrosslinked GelMA macromolecules. At day 3, the residual weight was 70 ± 3 %, 73 ± 5 % and 75 ± 7 % for GelMA 7.5 %, GelMA 7.5 %/0.1 nHA and GelMA 7.5 %/0.2 nHA, respectively. Then, the weight stabilized and remained constant up to 14 days, for all the formulations. In the cell culture medium, there was a significant weight loss (≈ 30 %) within 1 h for all the formulations ($p \leq 0.0001$). However, the overall 3D structural integrity was maintained, as after 1 h the weight loss was reduced, and gradually stabilized after day 3 (residual weight 67 ± 3 %, 69 ± 4 % and 69 ± 5 for GelMA 7.5 %, GelMA 7.5 %/0.1 nHA and GelMA 7.5 %/0.2 nHA, respectively), and up to day 14. No significant difference ($p > 0.05$) was observed among the formulations up to 14 days of incubation in the two media.

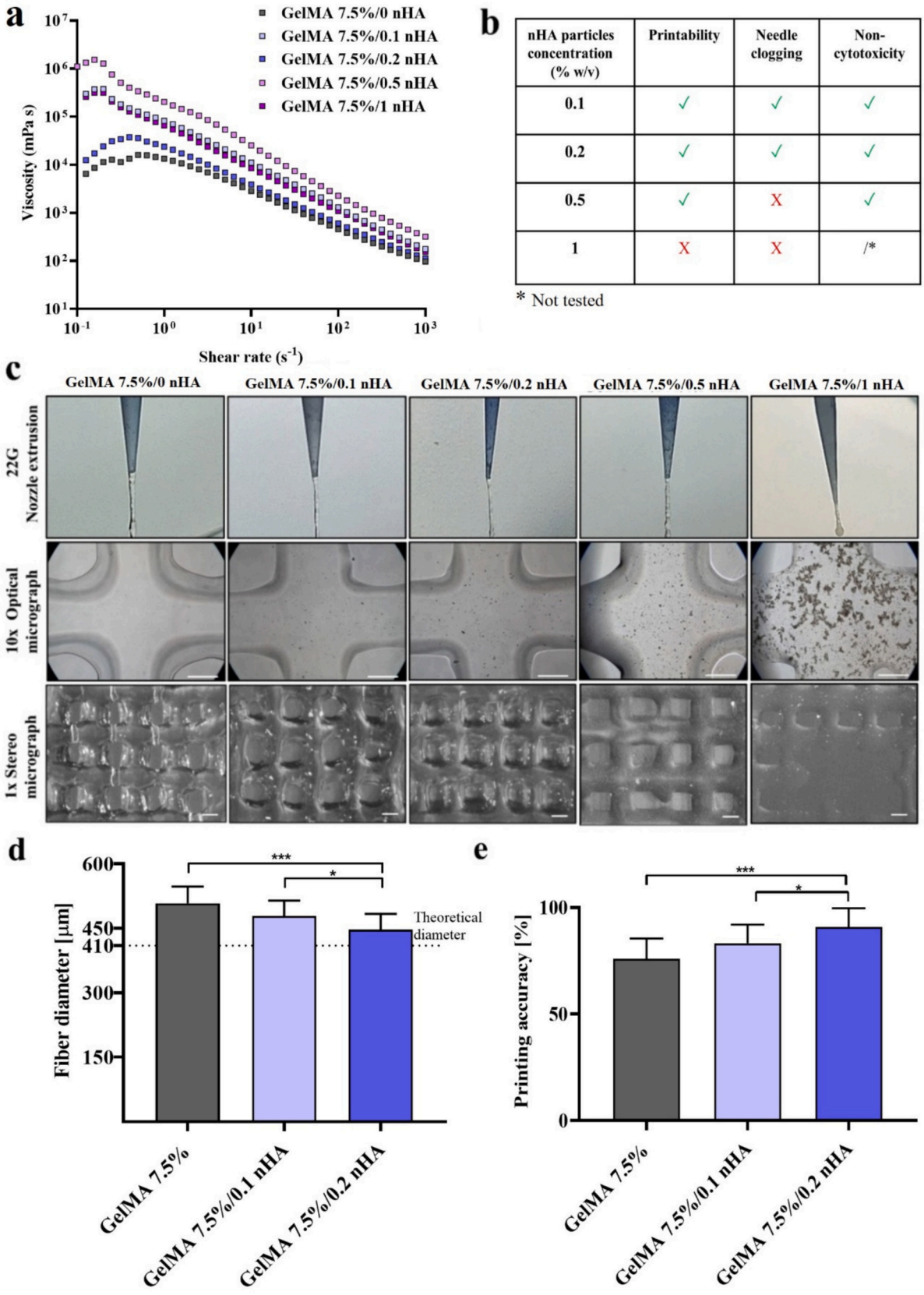

nHA particles concentration (% w/v)	Printability	Needle clogging	Non-cytotoxicity
0.1	✓	✓	✓
0.2	✓	✓	✓
0.5	✓	X	✓
1	X	X	/*

* Not tested

Fig. 3. GelMA 7.5 %/nHA inks and nHA effect on rheological and 3D printing properties. **(a)** Viscosity versus shear rate for GelMA 7.5 %/0 nHA and loaded with 0.1, 0.2, 0.5 and 1 nHA, measured at 22 °C. **(b)** Effect of the different nHA concentrations on printability, needle clogging and cytotoxicity. **(c)** Extrusion test (22 G needle) for GelMA w/wo nHA, top view of the 3D printed scaffold obtained by optical microscope (scale bar = 200 μm) and stereomicroscope (scale bar = 500 μm), **(d)** Fiber diameter measurements on GelMA 7.5 %, GelMA 7.5 %/0.1 nHA and GelMA 7.5 %/0.2 nHA, and compared to the theoretical diameter (i.e., needle size, 410 μm). **(e)** Printing accuracy evaluated for GelMA 7.5 %, GelMA 7.5 %/0.1 nHA and GelMA 7.5 %/0.2 nHA (* $p \leq 0.05$, *** $p \leq 0.001$).

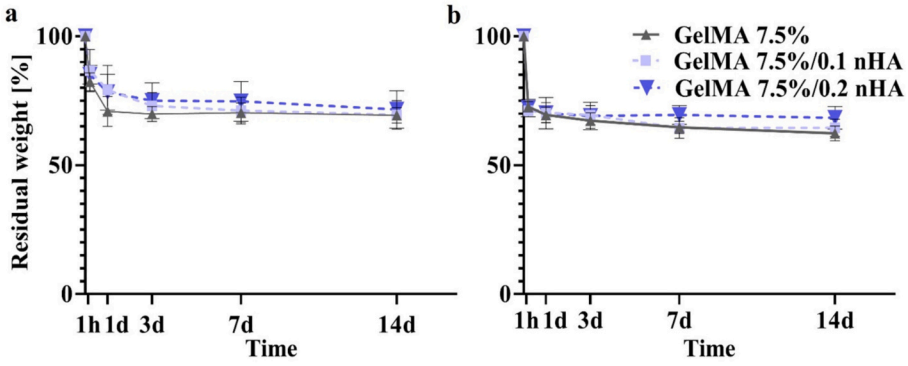

Fig. 4. Residual weight for GelMA 7.5 %, GelMA 7.5 %/0.1 nHA and GelMA 7.5 %/0.2 nHA in **(a)** dH2O, and **(b)** in IMDM cell culture medium over 14 d.

3.3. 3D bioprinting experiment

The 3D bioprinting experiments were performed using GelMA 7.5 % and GelMA 7.5 %/0.2 nHA. Saos-2 cells were homogeneously mixed with the inks to obtain GelMA 7.5 % and GelMA 7.5 %/0.2 nHA bioinks. The printing parameters used during the 3D bioprinting were the ones previously optimized, i.e., $P = 23$ kPa and $P = 26$ kPa, speed = 7 mm/s for GelMA 7.5 % and GelMA 7.5 %/0.2 nHA, respectively. Alamar Blue results showed a significant difference ($p < 0.0001$) in Saos-2 metabolic activity, higher for GelMA 7.5 %/0.2 nHA at all the considered timepoints (at day 7, $p \leq 0.001$) with a positive growing trend from day 3 to day 14 (Fig. 5(a)).

Concerning the Live-Dead assay, the quantification of viable cells demonstrated that cell viability was higher than 80 % for the two bioinks at all the timepoints (Fig. 5(b)), with a negligible percentage of dead cells. In addition, GelMA 7.5 %/0.2 nHA showed a higher number of viable cells, and this significant difference was sustained over time (Fig. 5(b)). Representative Live Dead staining images were acquired at the considered timepoints and showed a qualitative homogeneous distribution of viable cells around the pores and the overall geometry (Fig. 5(c)). The survival and proliferation trend of Saos-2 cells (Fig. 5(d)) resulted in a qualitative cell spreading within the constructs. Regarding the 3D bioprinted constructs geometry, some variations in fiber diameter and pores due to material loss over the entire culture time were observed (Fig. 5(e)). Both GelMA 7.5 % and GelMA 7.5 %/0.2 nHA experienced a fiber diameter shrinkage, with decreases of approximately 33 and 14 % on day 1, compared to GelMA and GelMA 7.5 %/0.2 nHA after 3D printing, respectively. As a result, this caused an expansion in pore size on day 1. The lower variability in fiber diameter for the GelMA 7.5 %/0.2 nHA constructs is related to the nHA presence, as previously observed [34,51]. Nonetheless the diameter variations in culture conditions, both GelMA 7.5 % and GelMA 7.5 %/0.2 nHA maintained the 3D bioprinted resulting geometry, and the constructs supported Saos-2 cells viability and proliferation over 14 days.

4. Discussion

The development of 3D bioprinted bone models for investigating pathological conditions and drug screening purposes is raising interest recently but no satisfying models exist yet, due to the difficulty in mimicking bone tissue properties [3,13,21,44]. In this study bone organic and inorganic phases are mimicked by GelMA and nHA, respectively.

Gelatin functionalization by methacryloyl substituent groups enables to photocrosslink gelatin by using a photoinitiator and a UV source, by which the photopolymerization of methacryloyl groups occurs. The methacrylation substitution of gelatin and UV crosslinking enable to overcome gelatin instability at body temperature and cytocompatibility issues related to other gelatin crosslinking agents (e.g., glutaraldehyde) [27]. Indeed, we demonstrated that UV crosslinking process did not affect cells attachment and metabolic activity. Therefore, the introduction of methacryloyl groups does not impact the RGD peptide, and the crosslinking process can be considered safe.

Regarding 3D printing, previous studies [27,35,67] have taken advantage of the thermo-responsive nature of GelMA, in which it behaves as gel below the sol-gel transition temperature, thus being suitable for extrusion through the needle during the printing process [28,51,65]. According to literature, the concentration range for GelMA printability is usually 5–15 % *w/v* [13,27,60,65]. The selection of GelMA concentration within this range depends on several variables (e.g., 3D printing system, final application, use of additives). However, literature studies [27,66,72] demonstrated that below 5 % *w/v*, GelMA shows low viscosity and limited 3D printing process, while above 10 % w/v GelMA printability could be challenging due to increase in gel viscosity and needle clogging issues. In our study, we assessed that GelMA 5 % and GelMA 10 % formulations were the printability boundaries as they resulted in weak and too viscous gels, respectively, and were thus excluded from our study. In accordance with our finding, some studies [27,67] observed reduced printability even for GelMA below 7 % w/v. Within the 5–10 % w/v GelMA printability boundaries, we obtained that GelMA 7.5 % was adequate in terms of extrudability and post-printing shape fidelity. This result is in accordance with previous reports [73–76]. The selected GelMA 7.5 % resulted biocompatible for Saos-2 cells and did not release potential cytotoxic by-products when maintained in culture medium. Indeed, the conditioned medium derived from GelMA 7.5 % positively influenced cell metabolic activity, with higher RFU values in comparison to cell maintained in fresh medium, demonstrating the absence of potential cytotoxic by-products.

The GelMA 7.5 % 3D printed structures showed acceptable printing accuracy (> 75 %), with the pores developed in the square-pattern lattice ranging 550–700 μm. Although the pores size in 3D printing relies on many different factors (i.e., design, fibers spacing, polymer concentration and printing parameters), the pores range obtained in this study is comparable to the optimal pores dimensions (ranging from 200 to 300 μm, and up to 1000 μm) obtained by previous studies using PU [3], collagen [19], PEG [18], PLLA [23] and GelMA [13] to develop 3D in vitro bone tumour models. Indeed, these previous studies demonstrated promising results in terms of cells colonization (both healthy and tumour cells), nutrients exchange and mechanical properties. To further enhance the biomimicry and obtain an ink with inorganic bone-like similar composition [77], stoichiometric nHA in the range 0.1–1 % w/v was added to GelMA. In literature, the nHA concentration range to be combined with hydrogels (i.e., GelMA, hyaluronic acid, chitosan) is variable (0.1–5 wt%) [34–37,78], and the suitability for extrusion-based 3D printing relies on the 3D printing setup (e.g., extrusion pressure, needle type and dimension) and on material properties (e.g., gel viscosity, nHA dimensions and aggregation behavior). Similar to our results, in [36] the nHA workable range was 0.1–0.75 wt%, with clogging

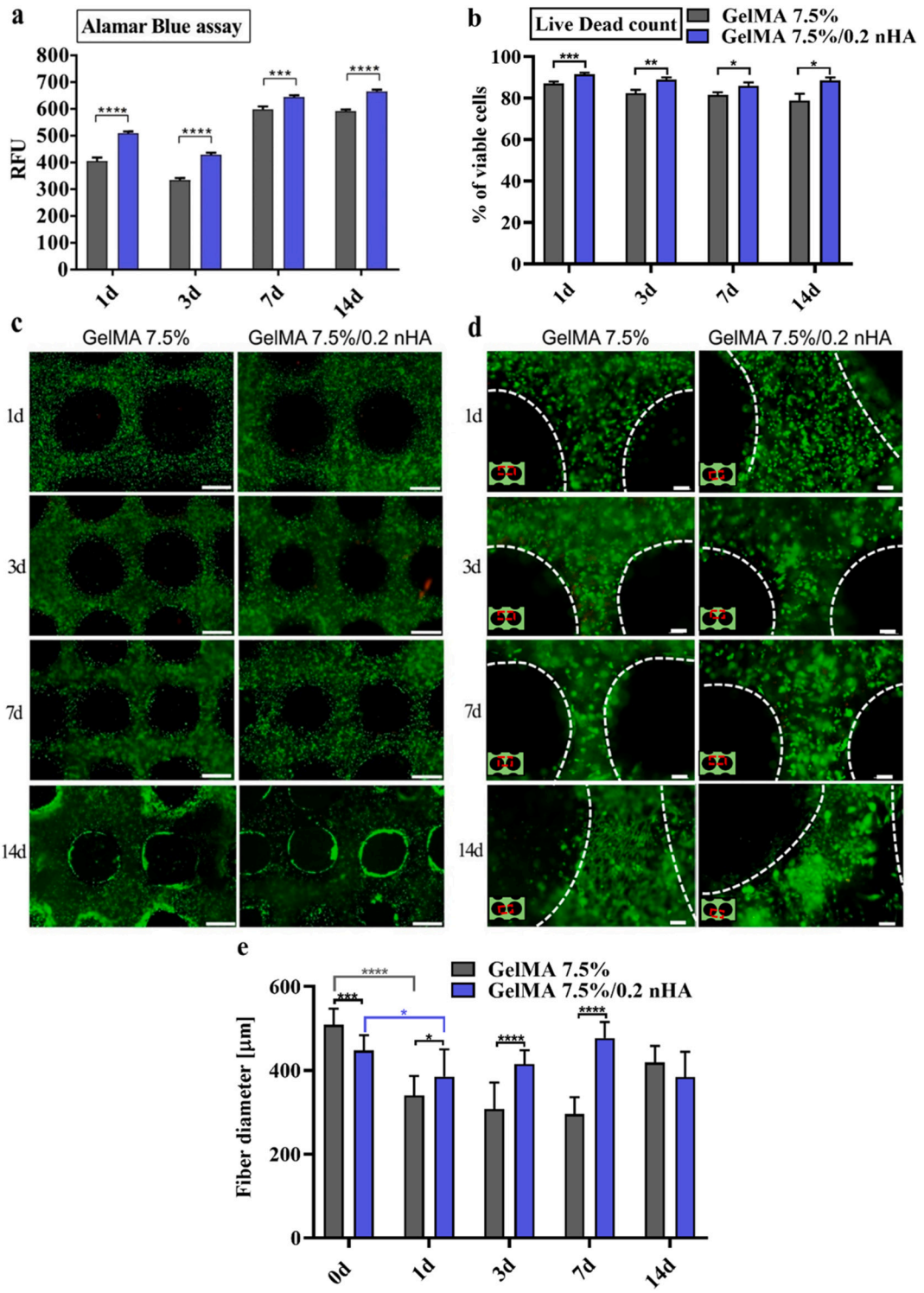

Fig. 5. GelMA 7.5 % and GelMA 7.5 %/0.2 nHA 3D bioprinting experiment. **(a)** Alamar Blue assay to evaluate cell metabolic activity after bioprinting at 1d, 3d, 7d and 14d. **(b)** Quantification of Saos-2 cells viability on Live Dead staining of cells visualized at 20× (* $p \leq 0.05$, ** $p \leq 0.01$, *** $p \leq 0.001$, **** $p \leq 0.0001$). **(c)** Representative images of pores of 3D bioprinted samples, 4×, Scale bar 500 µm **(d)** Representative image of the fiber of 3D bioprinted sample, with dotted lines indicating the pores, 10×, Scale bar 100 µm. **(e)** Fiber diameter measurements for GelMA 7.5 % and GelMA 7.5 %/0.2 nHA at d0 (after 3D printing process), and at 1d, 3d, 7d and 14d in culture conditions (* $p \leq 0.05$, *** $p \leq 0.001$, **** $p \leq 0.0001$). (For interpretation of the references to colour in this figure legend, the reader is referred to the web version of this article.)

of the 21 G needle (inner diameter = 510 µm) above 0.75 wt%. The inclusion of nHA, besides mimicking the bone native niche, is also crucial to control the physico-chemical and printability properties of the ink [13,34,37]. In our study, we found that increasing the nHA concentration (up to 0.2 % *w/v*) contributes to enhance the filament extrusion and the printing fidelity compared to pristine GelMA. However, we obtained that material extrusion was impaired for nHA concentrations equal to 0.5 % (*w/v*) and above, due to partial and severe needle clogging, respectively. Moreover, we did not observe a positive effect on Saos-2 cells proliferation by increasing nHA concentration to

0.5 % (w/v). As reported in the literature [35,36] and observed in our study, increasing nHA is feasible up to a certain threshold, as above certain range polymer and ceramic phase separation [35] was observed, leading to needle clogging and non-uniform extrusion of GelMA/nHA. However, as confirmed by the literature [33–35], nHA addition has a positive influence in terms of hydrogel properties and 3D printed shape even if used at low and narrow concentrations range. Regarding the stability behavior over time of 3D printed GelMA structures w/wo nHA, we did not observe significant difference at any timepoint due to the low nHA concentrations. Indeed, as reported in [35], nHA could show a positive effect on the stability of the 3D printed constructs for higher nHA concentrations (e.g., 1 and 3 % wt), as an increased residual mass ratio was observed. In our study, upon incubation in dH2O and IMDM, the 3D printed structures experienced significant weight and shape variations, mainly in IMDM. This led to the formation of thinner hydrogel fiber and larger pores diameter constituting the scaffold at different incubation times. This finding has been previously reported, and it could may be related to the influence of oxygen in hindering the UV effect, causing an impaired crosslinking at the hydrogel's surface and resulting in the material washing out after incubation [24,34]. During the culture time, the material loss could be enhanced due to cells, as they secrete factors (i.e., metalloproteinase) that contribute to enzymatic breakdown process, as previously observed [79,80]. However, we obtained that in presence of nHA, the pores experienced significant lower diameter variation during the in vitro 3D bioprinting experiment, thus highlighting the nHA beneficial effect in preserving the 3D printed shape. The higher stability of GelMA/nHA samples is likely due to the strong physical interactions occurring between GelMA and nHA, facilitated by the high surface-to-volume ratio of nHA, which provides more interaction sites with GelMA [81]. Additionally, nHA may act as a barrier against oxygen penetration, which could enhance crosslinking efficiency by reducing the presence of oxygen that might otherwise hinder the crosslinking process [82,83].

Concerning the biological assessment, the selection of inks compositions and 3D bioprinting process that guarantee the obtainment of viable and metabolically active cells is crucial to validate the model for further investigations. After 3D bioprinting process, a qualitative homogenous cell distribution in the samples was detected for both GelMA 7.5 % and GelMA 7.5 %/0.2 nHA and cell viability was maintained over 80 % for both the inks at all considered timepoints, consistent with data in literature regarding gelatin-based hydrogels and ceramic additives (i.e., nHA, bioactive glass) [13,84]. The presence of the used nHA concentrations was not cytotoxic for Saos-2 cells, and higher values of RFU were noticed in comparison to GelMA 7.5 %. The presence of 0.2 nHA regulates Saos-2 cancer cells behavior, supporting their adhesion and proliferation, as reported on osteosarcoma and breast cancer cells [38,57,85,86]. This positive effect may be related to nHA ability to modulate protein adsorption, thus contributing to enhanced cell proliferation [16]. Although this result needs to be further investigated, it confirms the importance of including HA in bone models. In addition, cell behavior was positively affected by the bioactivity of apatite, prevailing over the potential shear stress caused by the presence of nHA particles during bioprinting process, thus confirming that the needle-like shape of the HA particles appeared suitable for printing [57] and HA could be further included in 3D bioprinted complex 3D in vitro bone models. These data were also confirmed by the Live Dead assay. In fact, the quantification of cell viability by counting viable and dead cells showed high values of cell viability for all samples at all the timepoints, with a homogeneous cell distribution around the pores and a proliferation trend behavior at longer culture timepoints.

From these results, it can be asserted that the GelMA, GelMA/nHA formulations and the 3D printed structures do not release cytotoxic by-products and are able to guarantee Saos-2 cell viability over time, no matter the observed weight loss. Moreover, the proposed material formulations represent potentially suitable candidates for 3D bioprinted bone models, as they reproduce the native bone niche composition and show good results in terms of 3D printing/bioprinting suitability.

5. Conclusion

In this study, an osteomimetic GelMA 7.5 %/nHA ink was proposed, and its suitability for bioprinting was investigated in view of its application for future in vitro study of complex bone models. Focusing on the investigation of osteomimetic inks is important to increase the biomimicry level of the models. The selected GelMA 7.5 % and GelMA 7.5 %/nHA formulations showed suitable printability, and the 3D printing parameters were optimized to obtain accurate and reproducible structures. We observed that nHA positively influence the 3D printing accuracy and the post-printing shape fidelity in physiological conditions. Thus, we demonstrated that nHA allow to customize the inks and tune the ink behavior within a suitable concentration range. No cytotoxic effect was observed on Saos-2 cells, neither in GelMA alone, nor upon nHA addition. The 3D bioprinted scaffolds were able to preserve the shape and allow Saos-2 cell viability (> 80 %) over 14 days, both for GelMA 7.5 % and GelMA 7.5 %/0.2 nHA. Here, the presence of nHA not only has no detrimental effect on cells, but also exerts a beneficial influence, by enhancing cells metabolic activity and viability. Thus, the developed ink formulations are suitable to recreate a 3D bone-mimetic microenvironment and could potentially be used as in vitro platform for future disease models or drug screening purposes.

CRediT authorship contribution statement

Tiziana Fischetti: Writing – original draft, Methodology, Investigation, Formal analysis, Data curation, Conceptualization. **Gabriela Graziani:** Writing – review & editing, Methodology, Investigation, Conceptualization. **Giorgia Borciani:** Writing – original draft, Methodology, Formal analysis, Data curation, Conceptualization. **Matteo Pitton:** Writing – original draft, Methodology, Investigation, Formal analysis, Data curation. **Elisa Boanini:** Writing – review & editing, Validation, Resources. **Nicola Baldini:** Writing – review & editing, Validation, Resources, Conceptualization. **Silvia Farè:** Writing – review & editing, Validation, Supervision, Resources, Conceptualization.

Funding sources

This research did not receive any specific grant from funding agencies in the public, commercial, or not-for-profit sectors.

Declaration of competing interest

The authors declare no conflict of interest.

Appendix A. Supplementary data

Supplementary data to this article can be found online at https://doi.org/10.1016/j.bioadv.2025.214608.

Data availability

Data will be made available on request.

References

[1] T. Fischetti, G. Di Pompo, N. Baldini, S. Avnet, G. Graziani, 3D printing and bioprinting to model bone cancer: the role of materials and nanoscale cues in directing cell behavior, Cancers (Basel) 13 (16) (2021) 4065, https://doi.org/10.3390/cancers13164065.

[2] M. Cortini, N. Baldini, S. Avnet, New advances in the study of bone tumors: a lesson from the 3D environment, Front. Physiol. 10, no. JUN (2019) 1–8, https://doi.org/10.3389/fphys.2019.00814.

[3] N. Contessi Negrini, et al., An osteosarcoma model by 3D printed polyurethane scaffold and in vitro generated bone extracellular matrix, Cancers (Basel) 14 (2022) 2003, https://doi.org/10.3390/cancers14082003 [Online]. Available:.

[4] J.A. McGovern, M. Griffin, D.W. Hutmacher, Animal models for bone tissue engineering and modelling disease, DMM Dis. Model. Mech. 11 (4) (2018) 033084, https://doi.org/10.1242/dmm.033084.
[5] R. Owen, G.C. Reilly, In vitro models of bone remodelling and associated disorders, Front. Bioeng. Biotechnol. 6 (OCT) (2018) 1–22, https://doi.org/10.3389/fbioe.2018.00134.
[6] J.P. Vanderburgh, S.A. Guelcher, J.A. Sterling, 3D bone models to study the complex physical and cellular interactions between tumor and the bone microenvironment, J. Cell. Biochem. 119 (7) (2018) 5053–5059, https://doi.org/10.1002/jcb.26774.
[7] V. Angeloni, et al., Polyurethane foam scaffold as in vitro model for breast cancer bone metastasis, Acta Biomater. 63 (2017) 306–316, https://doi.org/10.1016/j.actbio.2017.09.017.
[8] S. Avnet, S. Lemma, M. Cortini, G. Di Pompo, F. Perut, N. Baldini, Pre-clinical models for studying the interaction between mesenchymal stromal cells and cancer cells and the induction of stemness, Front. Oncol. 9, no. APR (2019) 1–8, https://doi.org/10.3389/fonc.2019.00305.
[9] G. Domenici, R. Eduardo, H. Castillo-Ecija, G. Orive, Á.M. Carcaboso, C. Brito, Pdx-derived Ewing's sarcoma cells retain high viability and disease phenotype in alginate encapsulated spheroid cultures, Cancers (Basel) 13 (4) (2021) 1–18, https://doi.org/10.3390/cancers13040879.
[10] H. Zhong, L. Xuan, D. Wang, J. Zhou, Y. Li, Q. Jiang, Generation of a co-culture cell micropattern model to simulate lung cancer bone metastasis for anti-cancer drug evaluation, RSC Adv. 7 (35) (2017) 21837–21847, https://doi.org/10.1039/c7ra01868a.
[11] J. Ahn, et al., 3D microfluidic bone tumor microenvironment comprised of hydroxyapatite/fibrin comp, Front. Bioeng. Biotechnol. 7 (JUL) (2019) 1–13, https://doi.org/10.3389/fbioe.2019.00168.
[12] E.C. González Díaz, S. Sinha, R.S. Avedian, F. Yang, Tissue-engineered 3D models for elucidating primary and metastatic bone cancer progression, Acta Biomater. 99 (2019) 18–32, https://doi.org/10.1016/j.actbio.2019.08.020.
[13] X. Zhou, et al., 3D bioprinting a cell-laden bone matrix for breast cancer metastasis study, ACS Appl. Mater. Interfaces 8 (44) (2016) 30017–30026, https://doi.org/10.1021/acsami.6b10673.
[14] D. Wu, et al., A 3D-bioprinted multiple myeloma model, Adv. Healthc. Mater. 11 (7) (2022) 1–13, https://doi.org/10.1002/adhm.202100884.
[15] M. Khanmohammadi, M. Volpi, E. Walejewska, A. Olszewska, W. Swieszkowski, Printing of 3D biomimetic structures for the study of bone metastasis: a review, Acta Biomater. 178 (2024) 24–40, https://doi.org/10.1016/j.actbio.2024.02.046.
[16] W. Zhu, et al., A 3D printed nano bone matrix for characterization of breast cancer cell and osteoblast interactions, Nanotechnology 27 (31) (2016) 1–9, https://doi.org/10.1088/0957-4484/27/31/315103.
[17] H. Cui, et al., Engineering a novel 3D printed vascularized tissue model for investigating breast cancer metastasis to bone, Adv. Healthc. Mater. 9 (15) (2020) 1–11, https://doi.org/10.1002/adhm.201900924.
[18] W. Zhu, B. Holmes, R.I. Glazer, L.G. Zhang, 3D printed nanocomposite matrix for the study of breast cancer bone metastasis, Nanomed. Nanotechnol. Biol. Med. 12 (1) (2016) 69–79, https://doi.org/10.1016/j.nano.2015.09.010.
[19] E. Pellegrini, et al., A 3D collagen-based bioprinted model to study osteosarcoma invasiveness and drug response, Polymers (Basel) 14 (19) (2022) 4070, https://doi.org/10.3390/polym14194070.
[20] B. Holmes, W. Zhu, L.G. Zhang, Development of a novel 3D bioprinted in vitro nano bone model for breast cancer bone metastasis study, Mater. Res. Soc. Symp. Proc. 1724 (Figure 1) (2015) 1–6, https://doi.org/10.1557/opl.2014.941.
[21] K.A. Kwakwa, J.P. Vanderburgh, S.A. Guelcher, J.A. Sterling, Engineering 3D models of tumors and bone to understand tumor-induced bone disease and improve treatments, Curr. Osteoporos. Rep. 15 (4) (2017) 247–254, https://doi.org/10.1007/s11914-017-0385-9.
[22] A.R. Bastos, et al., Hydroxyapatite/alginate/gellan gum inks with osteoconduction and osteogenic potential for bioprinting bone tissue analogues, Int. J. Biol. Macromol. 271 (P2) (2024) 132611, https://doi.org/10.1016/j.ijbiomac.2024.132611.
[23] M.L. Wang, N.Y. Xu, R.Z. Tang, X.Q. Liu, A 3D-printed scaffold-based osteosarcoma model allows to investigate tumor phenotypes and pathogenesis in an in vitro bone-mimicking niche, Mater. Today Bio. 15 (May) (2022) 100295, https://doi.org/10.1016/j.mtbio.2022.100295.
[24] L. Bova, et al., A porous gelatin methacrylate-based material for 3D cell-laden constructs, Macromol. Biosci. 23 (2) (2023) 1–10, https://doi.org/10.1002/mabi.202200357.
[25] W. Zhu, M. Wang, Y. Fu, N.J. Castro, S.W. Fu, L.G. Zhang, Engineering a biomimetic three-dimensional nanostructured bone model for breast cancer bone metastasis study, Acta Biomater. 14 (2015) 164–174, https://doi.org/10.1016/j.actbio.2014.12.008.
[26] A. Pirosa, R. Gottardi, P.G. Alexander, R.S. Tuan, Engineering in-vitro stem cell-based vascularized bone models for drug screening and predictive toxicology, Stem Cell Res Ther 9 (2018) 112, https://doi.org/10.1186/s13287-018-0847-8.
[27] N. Celikkin, et al., In vitro and in vivo assessment of a 3D printable gelatin methacrylate hydrogel for bone regeneration applications, J Biomed Mater Res B Appl Biomater (March) (2022) 7–10, https://doi.org/10.1002/jbm.b.35067.
[28] G. Cidonio, et al., Osteogenic and angiogenic tissue formation in high fidelity nanocomposite Laponite-gelatin bioinks, Biofabrication 11 (3) (2019) 035027, https://doi.org/10.1088/1758-5090/ab19fd.
[29] Y. Yang, et al., Bioprinting of an osteocyte network for biomimetic mineralization, Biofabrication 12 (4) (2020) 045013, https://doi.org/10.1088/1758-5090/aba1d0.
[30] C. Mcbeth, J. Lauer, M. Ottersbach, J. Campbell, A. Sharon, A.F. Sauer-Budge, 3D bioprinting of GelMA scaffolds triggers mineral deposition by primary human osteoblasts, Biofabrication 9 (2017) 15009, https://doi.org/10.1088/1758-5090/aa53bd.
[31] J. Yin, M. Yan, Y. Wang, J. Fu, H. Suo, 3D bioprinting of low-concentration cell-laden gelatin methacrylate (GelMA) bioinks with a two-step cross-linking strategy, ACS Appl. Mater. Interfaces 10 (8) (2018) 6849–6857, https://doi.org/10.1021/acsami.7b16059.
[32] S. Chen, Y. Shi, X. Zhang, J. Ma, Biomimetic synthesis of Mg-substituted hydroxyapatite nanocomposites and three-dimensional printing of composite scaffolds for bone regeneration, J. Biomed. Mater. Res. - Part A 107 (11) (2019) 2512–2521, https://doi.org/10.1002/jbm.a.36757.
[33] Y. Wang, C. Lin, Study on properties of 3D-printed GelMA hydrogel scaffolds with different nHA contents, J. Bioact. Compat. Polym. 37 (5) (2022) 392–405, https://doi.org/10.1177/08839115221119211.
[34] A. Wenz, K. Borchers, G.E.M. Tovar, P.J. Kluger, Bone matrix production in hydroxyapatite-modified hydrogels suitable for bone bioprinting, Biofabrication 9 (4) (2017) 44103, https://doi.org/10.1088/1758-5090/aa91ec.
[35] S. Das, B. Basu, Extrusion-based 3D printing of gelatin mathacryloyl with nanocrystalline hydroxyapatite, Int. J. Appl. Ceram. Technol. 19 (2) (2022) 924–938, https://doi.org/10.1111/ijac.13885.
[36] J.C. Moses, T. Saha, B.B. Mandal, Chondroprotective and osteogenic effects of silk-based bioinks in developing 3D bioprinted osteochondral interface, Bioprinting 17 (June 2019) (2020) e00067, https://doi.org/10.1016/j.bprint.2019.e00067.
[37] T.T. Demirtaş, G. Irmak, M. Gümüşderelioğlu, A bioprintable form of chitosan hydrogel for bone tissue engineering, Biofabrication 9 (3) (2017) 035003, https://doi.org/10.1088/1758-5090/aa7b1d.
[38] S.P. Pathi, D.D.W. Lin, J.R. Dorvee, L.A. Estroff, C. Fischbach, Hydroxyapatite nanoparticle-containing scaffolds for the study of breast cancer bone metastasis, Biomaterials 32 (22) (2011) 5112–5122, https://doi.org/10.1016/j.biomaterials.2011.03.055.
[39] A. Sharma, et al., Investigating the role of sustained calcium release in silk-gelatin-based three-dimensional bioprinted constructs for enhancing the osteogenic differentiation of human bone marrow derived mesenchymal stromal cells, ACS Biomater Sci. Eng. 5 (2019) 1518–1533, https://doi.org/10.1021/acsbiomaterials.8b01631.
[40] T. Chen, Q. Zou, C. Du, C. Wang, Y. Li, B. Fu, Biodegradable 3D printed HA/CMCS/PDA scaffold for repairing lacunar bone defect, Mater. Sci. Eng. *C* 116 (April) (2020) 111148, https://doi.org/10.1016/j.msec.2020.111148.
[41] F. Nudelman, N.A.J.M. Sommerdijk, Biomineralization as an inspiration for materials chemistry, Angew. Chem. Int. Ed. 51 (27) (2012) 6582–6596, https://doi.org/10.1002/anie.201106715.
[42] K. Lin, C. Wu, J. Chang, Advances in synthesis of calcium phosphate crystals with controlled size and shape, Acta Biomater. 10 (10) (2014) 4071–4102, https://doi.org/10.1016/j.actbio.2014.06.017.
[43] H. Qiao, T. Tang, Engineering 3D approaches to model the dynamic microenvironments of cancer bone metastasis, Bone Res. 6 (3) (2018), https://doi.org/10.1038/s41413-018-0008-9.
[44] Y.S. Zhang, M. Duchamp, R. Oklu, L.W. Ellisen, R. Langer, A. Khademhosseini, Bioprinting the cancer microenvironment, ACS Biomater Sci. Eng. 2 (10) (2016) 1710–1721, https://doi.org/10.1021/acsbiomaterials.6b00246.
[45] J.L. Albritton, J.S. Miller, 3D bioprinting: improving in vitro models of metastasis with heterogeneous tumor microenvironments, DMM Dis. Model. Mech. 10 (1) (2017) 3–14, https://doi.org/10.1242/dmm.025049.
[46] N. Paxton, W. Smolan, T. Böck, F. Melchels, J. Groll, T. Jungst, Proposal to assess printability of bioinks for extrusion-based bioprinting and evaluation of rheological properties governing bioprintability, Biofabrication 9 (4) (2017) 44107, https://doi.org/10.1088/1758-5090/aa8dd8.
[47] S. Kyle, Z.M. Jessop, A. Al-Sabah, I.S. Whitaker, "Printability" of candidate biomaterials for extrusion based 3D printing: state-of-the-art, Adv. Healthc. Mater. 6 (16) (2017) 1–16, https://doi.org/10.1002/adhm.201700264.
[48] R. Levato, T. Jungst, R.G. Scheuring, T. Blunk, J. Groll, J. Malda, From shape to function: the next step in bioprinting, Adv. Mater. 32 (12) (2020) 1906423, https://doi.org/10.1002/adma.201906423.
[49] J. Groll, et al., A definition of bioinks and their distinction from biomaterial inks, Biofabrication 11 (2019) 013001, https://doi.org/10.1088/1758-5090/aaec52.
[50] L. Moroni, et al., Biofabrication strategies for 3D in vitro models and regenerative medicine, Nat. Publ. Group (2018), https://doi.org/10.1038/s41578-018-0006-y.
[51] N.B. Allen, B. Abar, L. Johnson, J. Burbano, R.M. Danilkowicz, S.B. Adams, 3D-bioprinted GelMA-gelatin-hydroxyapatite osteoblast-laden composite hydrogels for bone tissue engineering, Bioprinting 26, no. February (2022) e00196, https://doi.org/10.1016/j.bprint.2022.e00196.
[52] N.E. Vrana, et al., From 3D printing to 3D bioprinting: the material properties of polymeric material and its derived bioink for achieving tissue specific architectures, Cell Tissue Bank. 23 (3) (2022) 417–440, https://doi.org/10.1007/s10561-021-09975-z.
[53] D. van der Heide, G. Cidonio, M.J. Stoddart, M. D'Este, 3D printing of inorganic-biopolymer composites for bone regeneration, Biofabrication 14 (4) (2022) 042003, https://doi.org/10.1088/1758-5090/ac8cb2.
[54] S. Heid, A.R. Boccaccini, Advancing bioinks for 3D bioprinting using reactive fillers: a review, Acta Biomater. 113 (2020) 1–22, https://doi.org/10.1016/j.actbio.2020.06.040.
[55] P. Stolarov, J. de Vries, S. Stapleton, L. Morris, K. Martyniak, T.J. Kean, Suitability of gelatin methacrylate and hydroxyapatite hydrogels for 3D-bioprinted bone tissue, Materials (Basel). 17 (5) (2024) 1218, https://doi.org/10.3390/ma17051218.

[56] S. Jahangir, et al., Cell-laden 3D printed GelMA/HAp and THA hydrogel bioinks: development of osteochondral tissue-like bioinks, Materials 16 (2023) 7214, https://doi.org/10.3390/ma16227214. Online.
[57] T. Fischetti, et al., Incorporation / enrichment of 3D bioprinted constructs by biomimetic nanoparticles : tuning printability and cell behavior in bone models, Nanomaterials 13 (2023) 2040, https://doi.org/10.3390/nano13142040.
[58] M. Tschon, et al., Antiosteoporotic nanohydroxyapatite zoledronate scaffold seeded with bone marrow mesenchymal stromal cells for bone regeneration: a 3D in vitro model, Int. J. Mol. Sci. 23 (11) (2022) 5988, https://doi.org/10.3390/ijms23115988.
[59] M. Pitton, E. Ancona, S. Farè, Embedded 3D printing for the development of perfusable in vitro 3D model of soft tissue, Mater. Lett. 341 (July 2022) (2023) 134259, https://doi.org/10.1016/j.matlet.2023.134259.
[60] N. Celikkin, S. Mastrogiacomo, X. Frank Walboomers, W. Swieszkowski, Enhancing X-ray attenuation of 3D printed gelatin methacrylate (GelMA) hydrogels utilizing gold nanoparticles for bone tissue engineering applications, Polymers (Basel) 11 (2) (2019) 1–13, https://doi.org/10.3390/POLYM11020367.
[61] S.T. Bendtsen, S.P. Quinnell, M. Wei, Development of a novel alginate-polyvinyl alcohol-hydroxyapatite hydrogel for 3D bioprinting bone tissue engineered scaffolds, J. Biomed. Mater. Res. - Part A 105 (5) (2017) 1457–1468, https://doi.org/10.1002/jbm.a.36036.
[62] J. Schindelin, et al., Fiji: an open-source platform for biological-image analysis, Nat. Methods 9 (7) (2012) 676–682, https://doi.org/10.1038/nmeth.2019.
[63] G. Di Pompo, et al., Curcumin-loaded nanoparticles impair the pro-tumor activity of acid-stressed MSC in an in vitro model of osteosarcoma, Int. J. Mol. Sci. 22 (11) (2021) 5760, https://doi.org/10.3390/ijms22115760.
[64] J. Liu, L. Li, H. Suo, M. Yan, J. Yin, J. Fu, 3D printing of biomimetic multi-layered GelMA/nHA scaffold for osteochondral defect repair, Mater. Des. 171 (2019) 107708, https://doi.org/10.1016/j.matdes.2019.107708.
[65] B. Byambaa, et al., Bioprinted osteogenic and vasculogenic patterns for engineering 3D bone tissue, Adv. Healthc. Mater. 6 (16) (2017) 1–15, https://doi.org/10.1002/adhm.201700015.
[66] H.Y. N., Y.-W. C., Ming-You Shie, Jian-Jr Lee, Chia-Che-Ho, Ssu-Yin Yen, Effects of gelatin methacrylate bio-ink concentration on mechano-physical properties and human dermal, Polymers (Basel) 12 (2020) 1930, https://doi.org/10.3390/polym12091930 [Online]. Available:.
[67] T. Jain, et al., Impact of cell density on the bioprinting of gelatin methacrylate (GelMA) bioinks, Bioprinting 22 (January) (2021) e00131, https://doi.org/10.1016/j.bprint.2021.e00131.
[68] T. Billiet, E. Gevaert, T. De Schryver, M. Cornelissen, P. Dubruel, The 3D printing of gelatin methacrylamide cell-laden tissue-engineered constructs with high cell viability, Biomaterials 35 (1) (2014) 49–62, https://doi.org/10.1016/j.biomaterials.2013.09.078.
[69] M. Pitton, A. Fiorati, S. Buscemi, L. Melone, S. Farè, N. Contessi Negrini, 3D bioprinting of pectin-cellulose nanofibers multicomponent bioinks, Front. Bioeng. Biotechnol. 9 (December) (2021) 1–9, https://doi.org/10.3389/fbioe.2021.732689.
[70] N. Contessi Negrini, N. Celikkin, P. Tarsini, S. Farè, W. Święszkowski, Three-dimensional printing of chemically crosslinked gelatin hydrogels for adipose tissue engineering, Biofabrication 12 (2020) 025001, https://doi.org/10.1088/1758-5090/ab56f9.
[71] P.A. Amorim, M.A. D'Ávila, R. Anand, P. Moldenaers, P. Van Puyvelde, V. Bloemen, Insights on shear rheology of inks for extrusion-based 3D bioprinting, Bioprinting 22 (November 2020) (2021) e00129, https://doi.org/10.1016/j.bprint.2021.e00129.
[72] I. Pepelanova, K. Kruppa, T. Scheper, A. Lavrentieva, Gelatin-methacryloyl (GelMA) hydrogels with defined degree of functionalization as a versatile toolkit for 3D cell culture and extrusion bioprinting, Bioengineering 5 (2018) 55, https://doi.org/10.3390/bioengineering5030055.
[73] K. Ruberu, et al., Coupling machine learning with 3D bioprinting to fast track optimisation of extrusion printing, Appl. Mater. Today 22 (2021) 100914, https://doi.org/10.1016/j.apmt.2020.100914.
[74] D. Joung, et al., 3D printed stem-cell derived neural progenitors generate spinal cord scaffolds, Adv. Funct. Mater. 28 (39) (2018) 1801850, https://doi.org/10.1002/adfm.201801850.
[75] G. Ratheesh, C. Vaquette, Y. Xiao, Patient-specific bone particles bioprinting for bone tissue engineering, Adv. Healthc. Mater. 9 (23) (2020) 1–18, https://doi.org/10.1002/adhm.202001323.
[76] T. Anada, et al., Vascularized bone-mimetic hydrogel constructs by 3D bioprinting to promote osteogenesis and angiogenesis, Int. J. Mol. Sci. 20 (5) (2019) 1096, https://doi.org/10.3390/ijms20051096.
[77] E.C. González Díaz, A.G. Lee, L.C. Sayles, C. Feria, E.A. Sweet-Cordero, F. Yang, A 3D osteosarcoma model with bone-mimicking cues reveals a critical role of bone mineral and informs drug discovery, Adv. Healthc. Mater. 11 (17) (2022) 1–14, https://doi.org/10.1002/adhm.202200768.
[78] M. Huang, et al., 3D printing of GelMA/nanohydroxyapatite/melanin nanoparticles composite hydrogel scaffolds for bone regeneration through immunomodulation, Int. J. Biol. Macromol. 306 (P2) (2025) 141453, https://doi.org/10.1016/j.ijbiomac.2025.141453.
[79] S. Naahidi, et al., Biocompatibility of hydrogel-based scaffolds for tissue engineering applications, Biotechnol. Adv. 35 (5) (2017) 530–544, https://doi.org/10.1016/j.biotechadv.2017.05.006.
[80] Z. Xiao, et al., A peptide YGDEY from Tilapia gelatin hydrolysates inhibits UVB-mediated skin photoaging by regulating MMP-1 and MMP-9 expression in HaCaT cells, Photochem. Photobiol. 95 (6) (2019) 1424–1432, https://doi.org/10.1111/php.13135.
[81] T. Thakur, et al., Photocrosslinkable and elastomeric hydrogels for bone regeneration, J. Biomed. Mater. Res. - Part A 104 (4) (2016) 879–888, https://doi.org/10.1002/jbm.a.35621.
[82] K.S. Lim, J.H. Galarraga, X. Cui, G.C.J. Lindberg, J.A. Burdick, T.B.F. Woodfield, Fundamentals and applications of photo-cross-linking in bioprinting, Chem. Rev. 120 (19) (2020) 10662–10694, https://doi.org/10.1021/acs.chemrev.9b00812.
[83] W. Wang, et al., Fabrication of acid-swollen collagen fiber-based composite films: effect of nano-hydroxyapatite on packaging related properties, Int. J. Food Prop. 20 (5) (2017) 968–978, https://doi.org/10.1080/10942912.2016.1190745.
[84] M. Neufurth, et al., Engineering a morphogenetically active hydrogel for bioprinting of bioartificial tissue derived from human osteoblast-like SaOS-2 cells, Biomaterials 35 (31) (2014) 8810–8819, https://doi.org/10.1016/j.biomaterials.2014.07.002.
[85] A.S.M. Sikora, K. Marcinkowska, K. Marycz, R. Wiglusz, The potential selective cytotoxicity of poly (L- lactic acid)-based scaffolds functionalized with Nanohydroxyapatite and europium (III) ions toward osteosarcoma cells, Materials (Basel). 12 (22) (2019) 3779, https://doi.org/10.3390/ma12223779 [Online]. Available:.
[86] G. Borciani, G. Montalbano, P. Melo, N. Baldini, G. Ciapetti, C. Vitale-Brovarone, Assessment of collagen-based nanostructured biomimetic systems with a co-culture of human bone-derived cells, Cells 11 (26) (2022) 11010026, https://doi.org/10.3390/cells11010026.